Detecting molecular vibrational modes of side chains and endpoints in nanoscale proteins with graphene plasmon

Chenchen Wu(吴晨晨)[1,3#], Ning Liu(刘宁)[1,3#], Hai Hu(胡海)[1,3], Xiangdong Guo(郭相东)[1,3], Baoxin Liao(廖宝鑫)[1,3], Jiaming Liu(刘佳明)[2,3], Liming Wang(王黎明)[4], Chunying Chen(陈春英)[2,3], Xiaoxia Yang(杨晓霞)[1,3], and Qing Dai(戴庆)[1,3*]**

[1] *Division of Nanophotonics, CAS Center for Excellence in Nanoscience, National Center for Nanoscience and Technology, Beijing 100190, P. R. China.*

[2] *CAS Key Laboratory for Biomedical Effects of Nanomaterials & Nanosafety, National Center for Nanoscience and Technology of China, Beijing 100190, P. R. China.*

[3] *Center of Materials Science and Optoelectronics Engineering, University of Chinese Academy of Sciences, Beijing 100049, P. R. China.*

[4] *Institute of High Energy Physics, Chinese Academy of Sciences, Beijing 100049, P. R. China*

[#] *These authors contributed equally to this work.*

**Corresponding author: daiq@nanoctr.cn; ** corresponding author: yangxx@nanoctr.cn.*

Received Month X, XXXX; accepted Month X, XXXX; posted online Month X, XXXX

Abstract: Monitoring the chemical and structural changes in protein side chains and endpoints by infrared spectroscopy is important to study the chemical reaction and physical adsorption process of proteins. However, the detection of side chains and endpoints in nanoscale proteins is still challenging due to its weak infrared response. Here, by designing a double-layered graphene plasmon sensor on MgF_2/Si substrate in the IR fingerprint region, we detect the vibrational modes in side chains and endpoints (1397 cm^{-1} and 1458 cm^{-1}) of monolayer protein. The sensor could be applied on biochemistry to investigate the physical and chemical reaction of biomolecules.
OCIS Codes: 240.6680, 300.6340, 160.4236
doi:10.3788/COL-18-0715.R1

The identification and structure determination of protein, is of great importance to study its biofunctions, interactions and reactions [1]. Currently, there are several techniques which can provide the structural information of proteins, such as X-ray diffraction [2], Nuclear Magnetic Resonance (NMR) [3], cryo-electron microscopy [4], circular dichroism [5], Infrared (IR) spectroscopy [6,7] and so on. X-ray diffraction can provide high resolution structure for protein crystals, but there are plenty of proteins cannot be crystallized [2, 8]. NMR can measure the protein structures and investigate binding of proteins and small molecules; however, it is limited to relatively small proteins (molecular weight below 3000 in general) and needs large amounts of protein [6]. Although cryo-electron microscopy can give high resolution structures of very small samples in physiological state, it is still haunted by low signal to noise ratio, time-consuming sample preparation and it is costly [4]. Circular dichroism needs complex data analysis. Thus, IR spectroscopy is the most convenient one with least demanding both in terms of sample and time requirements among all these methods.

IR spectroscopy is hard to detect nanoscale proteins directly due to their weak light-matter interaction. By taking the advantage of plasmonic near-field enhancement to largely increase the interaction of molecules and the IR light, surface enhanced IR spectroscopy provides a sensitive method to identify nanoscale proteins as well as protein adsorption processes. [9-12] However, the detection of side chains and endpoints in nanoscale proteins is still challenging due to their weak IR response as well as the lack of plasmonic enhancement in the IR fingerprint region. The side chains and endpoints are closely related to protein chemical reaction and physical adsorption.[13-16] For example, the protonation state of most side chains can be reflected in the IR spectrum, such as protonation of Asparagine and Glutamine residues accompanies proton pumping by bacteriorhodopsin[17], electron transfer reactions and Ca^{2+} release from the Ca^{2+} ATPase [18]. However, due to their weak IR response as well as the lack of plasmonic enhancement in the IR fingerprint region, the detection of the side chains and endpoints of nanoscale proteins is still challenging.

Two-dimensional material, such as graphene, black phosphorus and MoS_2 have demonstrated exotic photonic properties such as strong light-matter interaction and electrical tunability [19-22], and has been widely used in waveguide, laser, IR sensor, polarizer and so on [23- 25]. Graphene plasmon is used to enhanced IR spectroscopy for detecting nanoscale materials due to its ultra-high IR light confinement and electrically tunability [26, 27]. For example, a high-sensitivity plasmonic biosensor for label-free detection of protein monolayers was demonstrated [28]. But due to the strong absorption of the substrate phonons, the signal of side chains in the fingerprint region have not been observed. Here, we adopt IR transparent substrate MgF_2 and double layered graphene to achieve high plasmonic enhancement in the fingerprint region and detect the side chains and endpoints of nanoscale protein. This kind of sensor supplies a convenient method to monitor both the backbone and side chains of nanoscale proteins which can be used in investigation the chemical reaction and physical adsorption of proteins.

The double layered graphene plasmon molecular fingerprint sensor is illustrated in Figure 1a. Plasmons can be excited in the double layered graphene nanoribbons (GNR) by focused IR beam, which result highly confined electromagnetic field that can enhance the IR absorption of nanoscale proteins [27-29]. The devices are fabricated as follows. A 700nm thick MgF_2 thin film was evaporated on low-doped Si substrate as IR transparent substrate and back gate for the graphene devices. We use MgF_2 film instead of traditional SiO_2 film as dielectric due to that MgF_2 has no active phonon absorption in the IR spectral range which can maintain the undisturbed high electromagnetic field enhancement in the fingerprint region. Two graphene layers

were transferred onto the MgF_2/Si substrate by repeating a wet-transfer method [30] Then electrically continuous GRN were fabricated in the double layered graphene via electron beam lithography (EBL) and oxygen ion etching. Au electrodes were deposited on to the GRN via a second EBL process and electron beam evaporation. For comparison, similar devices were fabricated with one layer graphene. Figure 1b displays a typical scanning electron microscope (SEM) image of the GNR, which shows uniform width and well-defined edges. The ribbon-to-pitch ratio of the ribbon array is 2.5, and the high density of the graphene nanoribbons is designed to achieve high plasmon extinction strength. The electrostatic tunability of the double layered graphene/MgF_2 device was tested and the electric transfer curve is shown in Figure 1c. The charge neutral point (CNP) of double layered graphene is at V_g of about 6 V. The

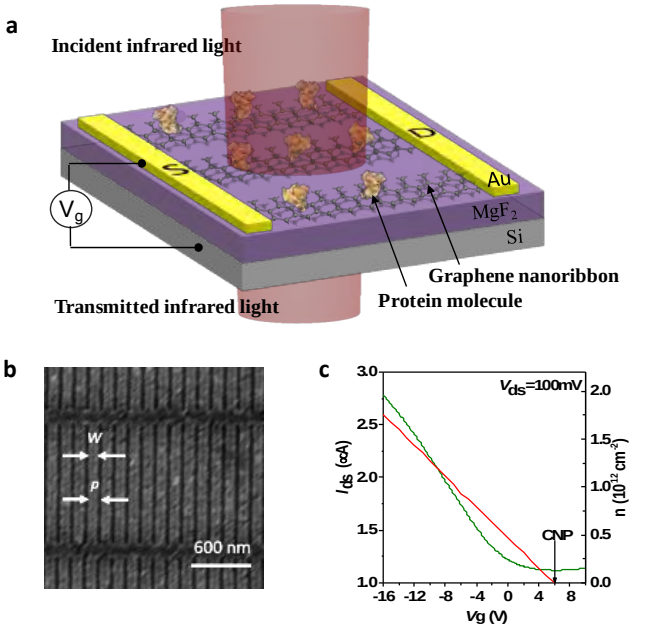

Figure 1. Graphene plasmon bio-sensor. (a) Schematic of the graphene plasmon sensor. Monolayer protein was deposited on top of the GNR array fabricated on 700 nm thick MgF_2 supported on Si substrate. Incident IR light excites plasmon resonance across the GNR, S, source; D, drain. **(b)** SEM image of a GNR array with a ribbon width (W) of 100 nm and a period width (P) of 140 nm. **(c)** The electric transfer curve (green curve) and carrier density (red line) of the double layered graphene/MgF_2 sensor, and the black arrow is the charge neutral point.

graphene carrier density can be tuned up to 1.8 x 10^{12} cm^{-2} at V_g= -16 V. Detail calculation is in the supplementary information.

In experiment, the plasmonic response of the double layered graphene nanoribbons was characterized using a Fourier transform infrared microscopy (FTIR). The transmission spectra of the graphene nanoribbon arrays at CNP (T_{CNP}) were used as background spectra, then the transmission spectra (T_{EF}) at certain Fermi levels E_F were collected to obtain the plasmonic extinction spectra T=1-T_{EF}/T_{CNP}. At same graphene ribbon width and bias voltage, the typical extinction spectra of the double layered graphene nanoribbon devices as well as the monolayer devices are shown in Figure 2a. They both have one prominent peak, indicating no substrate phonon effects from the MgF_2 substrate. However, the extinction peak of double layered graphene is much higher than the single layer graphene at Vg= -8 V, because the Fermi level of double layered graphene is the

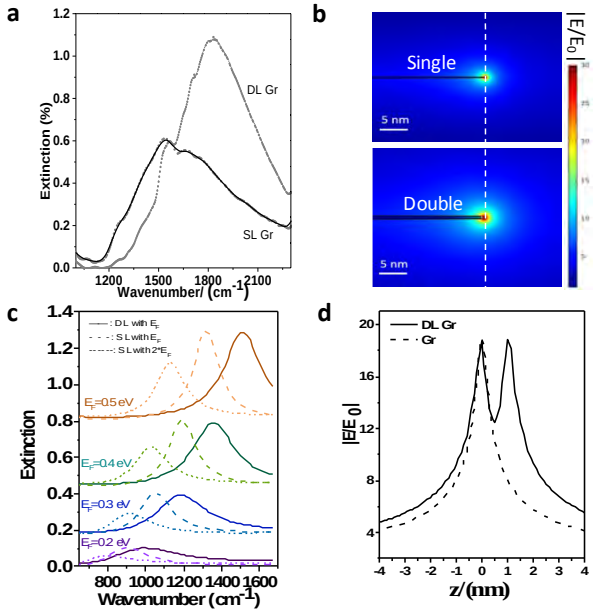

Figure 2. Comparison between double layered graphene plasmon and single layer graphene plasmon. (a) Experimental extinction spectra comparison between single layer graphene and double layered graphene at Vg=-8 V. Ribbon width, 100 nm. Period, 140 nm. **(b)** Simulated near-field enhancement distribution $|E/E_0|$ at the edge of single layer graphene (1000 cm^{-1}) and double layered graphene (1350 cm^{-1}) GNRs at their resonant frequencies. **(c)** Simulated extinction spectra of double layered graphene GNR with E_F, single layer graphene with $|E_F|$ and $2*|E_F|$. Fermi level E_F=0.2, 0.3, 0.4, 0.5 eV. **(d)** Near field enhancement distribution $|E/E_0|$ along the white dashed line in (b), E_F=0.3eV, mobility is using 600cm^2/(V*s)

sum of two single layer graphene at same bias voltage [29]. By using finite-element method, we simulate the electric field distribution for the graphene nanoribbons at the plasmon resonance frequency. As illustrated in Figure 2b, the field hotspots are located along the edges of the graphene nanoribbons, and the separation distance between two graphene layers is set as 1 nm. The cross section of the hot spot at the double layered graphene nanoribbon is much larger than that of the monolayer graphene nanoribbon. When each layer of double layered graphene has the same initial carrier density as n^{1L}, the simulation results in Figure 2c show that the extinction of double layered graphene plasmon is higher than single layer graphene plasmon and the peak is shifted to higher frequency at same Fermi level E_F and ribbon width. Then we apply $2*E_F$ (E_F=0.2, 0.3, 0.4, 0.5 eV) on single layer graphene, the simulated extinction strength of single layer graphene plasmon is generally same as the strength of double layered graphene plasmon with E_F. It can be explained by Drude model of graphene conductivity[29, 32]:

$$\delta(\omega) = \frac{i v_F e^2 \sqrt{\pi n}}{\hbar \pi \ (\omega + i\Gamma)},$$

where v_F is the Fermi velocity, n is carrier density, ω is the frequency and Γ is the scattering rate. Because $\delta = \delta 1 + \delta 2$ and $EF = \hbar v_F \sqrt{\pi n}$, we can conclude $E_F^{2L} = |E_F^1| + |E_F^2| = 2*E_F$ (when $E_F^1 = E_F^2$); the reason of double layered graphene plasmon extinction moving towards higher frequency is the coupling between two graphene layers [33]. For quantitative examination,

the convolution of the near field enhancement distribution with the perpendicular distance from the ribbon edge (along the dashed line in Figure 2b, 0.5 nm away from the ribbon edge) is shown in Figure 2d. It indicates that the optical enhancement and field distribution in double layered graphene ribbons is like to the single layer graphene ribbons. Both of experiment and simulation results show that the double layered graphene plasmon can provide more effective optical enhancement rather than the single layer graphene plasmon for the higher doping and broader tunability.

Bovine serum albumin (BSA), a kind of protein derived from cows which is often used as protein concentration standard in lab, was selected as an example to demonstrate the performance of double layered graphene biosensor. Monolayer proteins films (about 9 nm thick) were spin-coated onto the graphene devices as well as a spare substrate. A typical plasmonic extinction spectrum obtained after the protein layer-coating is shown in Figure 3a (red curve). As a comparison, the pristine IR absorption of the protein monolayer taken on the spare substrate is also displayed in Figure 3a (black curve). The IR absorption of the protein monolayer without plasmon enhancement is very weak and only the strongest peaks i.e. the amide I and amide II (marked as C and D) can be distinguished from the background noise due to the weak light-molecule interaction. In striking contrast to the noisy results without plasmon enhancement, the extinction spectrum of the same protein film covering the double layered graphene nanoribbon array features additional strong dips at A and B besides at the C and D. The dip behaviors in the plasmonic extinction peak are originated from destructive interference when the graphene plasmons and BSA's vibrational modes interact with an opposite phase relationship [31-35]. These dips can be assigned to the molecular fingerprints of the protein molecules. Partially representative molecular structure of BSA and assignments of vibrational fingerprints of BSA is illustrated in Figure 3b; BSA containing a peptide bond (-CO-NH-) which is the major part of the protein backbone at C and D, a carboxyl-terminal end at A (-OH) and a side chain at B (-CH_3) [34]. It indicates that not only the proteins backbone but also side chains vibrational modes are detected by the graphene plasmon sensor. It is the first time that the side chains and endpoints vibrational modes (1397 cm^{-1} and 1458 cm^{-1}) in fingerprint range of nanoscale proteins are detected by IR sensor.

Extinction spectra of the graphene nanoribbon array after the protein layer formation at different gate voltages are shown as solid lines in Figure 3c. For the evaluation of the signal enhancement, plasmonic enhanced molecular vibrational signals were extracted from the extinction spectra of the graphene nanoribbon arrays with the protein layer (solid lines) by subtracting the extinction spectra obtained without protein layer (dashed lines). The extracted signals are shown in Figure 3d. The enhancement is calculated via the subtraction of enhanced signal and origin protein signal and then divided by origin protein signal. The signal strength of vibrational modes gradually increase and the enhancement factors increase from 1.6 to 2.6 times, because the graphene plasmon resonance frequency is gradually approaching the enhanced modes by tuning ΔCNP from -11 V to -15 V. The double layered graphene plasmon broadband electrical tunability and higher doping offers adjustable enhancement at different modes, which could be used to monitor physicochemical changes in protein backbones, endpoints and side chains.

We detected both the protein backbone and side chains of monolayer protein film by using the undisturbed double layered graphene plasmon enhanced IR spectroscopy. Experimental results combined with the numerical simulation show that the double layered graphene plasmon has nearly doubled the cross section of monolayer graphene plasmon. By using the double layered graphene plasmon device with IR transparent substrate as IR sensor, the protein backbone (N-H+C-N, C=O) is enhanced by about 1.6-2.6 times and the side chains and endpoints (-CH_3, -COOH) of 9 nm thick BSA can be identified, which cannot be detected without the plasmonic enhancement. This work paves the way for monitoring the behavior of nanomaterial and chemical reaction or absorption that occur on endpoints and side chains as well as the physical change of the protein backbone, such as the interaction between proteins and nanomaterial medicine carrier and so on.

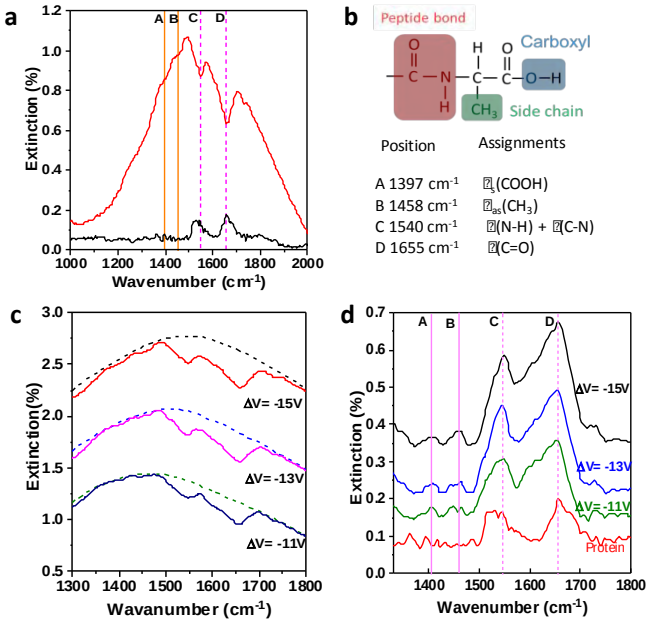

Figure 3. Enhanced infrared spectroscopy of nanoscale proteins. **(a)** Extinction spectrum of the GRN (Δ^{CNP} = -15 V) after the protein layer formation (red curve). The pristine extinction spectrum of a 9nm thick protein layer is shown as the black curve. The pink vertical lines indicate the vibrational fingerprints of backbone (A and B) while the orange ones correspond to side chain and endpoint (C and D). **(b)** Partially representative molecular structure of BSA, containing a peptide bond, a carboxyl-terminal end and a side chain (CH_3 is taken as an example); Vibrational fingerprints of BSA and their positions in (a). **ν**: stretching vibration, **νs**: symmetric stretching vibration, **δ**: in plane bending vibration, **δas**: asymmetric in plane bending vibration. "+" denotes the coupling between different vibration modes and the former contributes more than the latter. **(c)** Extinction spectra of the GNR after the protein layer formation at different gate voltages (solid lines). The baselines derived from the pristine plasmon extinction spectra are shown as dashed lines. **(d)** The plasmonic enhanced signal at different effective gate voltages were obtained by subtracting the corresponding baseline from each measured extinction

Funding Sources. This work is supported by the National Basic Key Research Program of China (Grant No. 2015CB932400), the National Key Research and Development Program of China (Grant No. 2016YFA0201600), the National

Natural Science Foundation of China (Grant Nos. 11504063, 11674073, 11704085, 11427808), the Bureau of International Cooperation, the key program of the Bureau of Frontier Sciences and Education, Chinese Academy of Sciences (QYZDB-SSW-SLH021), and Key Project of Chinese Academy of Sciences (ZDBS-SSW-JSC002).

References

1. Baker, D., & Sali, A. Protein structure prediction and structural genomics. *Science*, *294*(5540), 93-96 (2001).

2. Wlodawer, A., Bott, R., and Sjoh, L. The refined crystal structure of ribonuclease A at 2.0 A resolution. *J. Biol. Chem.*, 257: 1325–1332 (1982).

3. Braun, W. Distance geometry and related methods for protein structure determination from NMR data. *Q. Rev. Biophys.*, 19: 115–157 (1987).

4. Zhang, W., Chipman, P. R., Corver, J., Johnson, P. R., Zhang, Y., Mukhopadhyay, S., & Kuhn, R. J. Visualization of membrane protein domains by cryo-electron microscopy of dengue virus. *Nat. Struct. Mol. Biol*, *10*(11), 907 (2003).

5. Manavalan, P., & Johnson Jr, W. C. Sensitivity of circular dichroism to protein tertiary structure class. *Nature*, *305*(5937), 831 (1983).

6. Anker JN, Hall WP, Lyandres O, Shah NC, Zhao J et al. Biosensing with plasmonic nanosensors. *Nat. Mater.* 2008; 7: 442–453.

7. Yanik AA, Huang M, Kamohara O, Artar A, Geisbert TW et al. An optofluidic nanoplasmonic biosensor for direct detection of live viruses from biological media. *Nano Lett.* 2010; 10: 4962–4969.

8. Wang, L. M., Li, J. Y., Pan, J., Jiang, X. M., Ji, Y. L., Li, Y. F., Qu, Y., Zhao, Y. L., Wu, X. C. & Chen, C. Y. Revealing the Binding Structure of the Protein Corona on Gold Nanorods Using Synchrotron Radiation-Based Techniques: Understanding the Reduced Damage in Cell Membranes. *J. Am. Chem. Soc.* 2013, *135*, 17359-17368.

9. Aboul-Enein, Y., Bunacio, A. A., & Fleschin, S. Evaluation of the protein secondary structures using Fourier Transform Infrared Spectroscopy. *Gazi University Journal of Science*, *27*(1), 637-644 (2014).

10. Wang, L., Yan, L., Liu, J., Chen, C. & Zhao, Y. Quantification of Nanomaterial/Nanomedicine Trafficking in vivo. *Anal. Chem.*, *90*, 589-614 (2018).

11. Barth, A. Infrared spectroscopy of proteins. Biochim. Biophys. Acta 1767, 1073–1101 (2007).

12. Kauffmann, E., Darnton, N. C., Austin, R. H., Batt, C. & Gerwert, K. Lifetimes of intermediates in the b-sheet to a-helix transition of b-lactoglobulin by using a diffusional IR mixer. Proc. *Natl Acad. Sci.* USA 98, 6646–6649 (2001).

13. Stuart, B. H. Infrared Spectroscopy: Fundamentals and Applications (Wiley Online Library, 2005).

14. Heinz. F and Werner. M. Infrared Spectroscopy of Proteins. DOI:10.1002/9780470027325.s8201 (2006).

15. A. Barth, IR spectroscopy, in: V.N. Uversky, E.A. Permyakov (Eds.), Protein Structures: Methods in Protein Structure and Stability Analysis, Nova Science Publishers, 2006.

16. Barth, A. The infrared absorption of amino acid side chains. *Progress in Biophysics and Molecular Biology*, *74*(3-5), 141-173 (2000).

17. Zscherp, C. & Heberle, J. Infrared difference spectra of the intermediates L, M, N, and O of the Bacteriorhodopsin photoreaction obtained by time-resolved attenuated total reflection spectroscopy. *J. Phys. Chem. B* 101, 10542–10547 (1997).

18. Barth, A., Mäntele, W., & Kreutz, W. Infrared spectroscopic signals arising from ligand binding and conformational changes in the catalytic cycle of sarcoplasmic reticulum calcium ATPase. *Biochimica et Biophysica Acta (BBA)-Bioenergetics*, *1057*(1), 115-123 (1991).

19. Liu, Y., Sun, T., Ma, W., Yu, W., Nanjunda, S. B., Li, S., & Bao, Q. Highly responsive broadband black phosphorus photodetectors. *Chinese Optics Letters*, *16*(2), 020002. (2018).

20. Dhanabalan, S. C., Ponraj, J. S., Guo, Z., Li, S., Bao, Q., & Zhang, H. Emerging trends in phosphorene fabrication towards next generation devices. *Advanced Science*, *4*(6), 1600305 (2017).

21. Novoselov, K. S., Mishchenko, A., Carvalho, A., & Neto, A. C. 2D materials and van der Waals heterostructures. *Science*, *353*(6298), aac9439. (2016).

22. Dhanabalan, S. C., Ponraj, J. S., Zhang, H., & Bao, Q. Present perspectives of broadband photodetectors based on nanobelts, nanoribbons, nanosheets and the emerging 2D materials. *Nanoscale*, *8*(12), 6410-6434 (2016).

23. Bao, Q., Zhang, H., Wang, B., Ni, Z., Lim, C. H. Y. X., Wang, Y. & Loh, K. P. Broadband graphene polarizer. *Nat. Photon.* *5*(7), 411 (2011).

24. Bao, Q., Zhang, H., Wang, Y., Ni, Z., Yan, Y., Shen, Z. X. & Tang, D. Y. Atomic-layer graphene as a saturable absorber for ultrafast pulsed lasers. *Advanced Functional Materials*, *19*(19), 3077-3083 (2009).

25. Tang, P., Tao, Y., Mao, Y., Wu, M., Huang, Z., Liang, S., Chen, X., Qi, X., Huang, B., Liu, J. & Zhao, C. Graphene/MoS_2 heterostructure: a robust mid-infrared optical modulator for Er 3+-doped ZBLAN fiber laser. *Chinese Optics Letters*, *16*(2), 020012 (2018).

26. Garczarek, F. & Gerwert, K. Functional waters in intraprotein proton transfer monitored by FTIR difference spectroscopy. *Nature* 439, 109–112 (2006).

27. H. Hu, X. Yang, F. Zhai, D. Hu, R. Liu, K. Liu, Z. Sun and Q. Dai. *Nat. Commu.*, 2016, 7, 12334.

28. Rodrigo, D., Limaj, O., Janner, D., Etezadi, D., De Abajo, F. J. G., Pruneri, V., & Altug, H. Mid-infrared plasmonic biosensing with graphene. *Science*, *349*(6244), 165-168 (2015).

29. Rodrigo, D., Tittl, A., Limaj, O., De Abajo, F. J. G., Pruneri, V., & Altug, H. Double-layer graphene for enhanced tunable infrared plasmonics. *Light: Science & Applications*, 6(6), e16277 (2017).

30. Kim, S., Shin, S., Kim, T., Du, H., Song, M., Lee, C., & Seo, S. Robust graphene wet transfer process through low molecular weight polymethylmethacrylate. *Carbon*, *98*, 352-357 (2016).

31. Yan, H., Low, T., Zhu, W., Wu, Y., Freitag, M., Li, X. & Xia, F. Damping pathways of mid-infrared plasmons in graphene nanostructures. *Nat. Photon.*, *7*(5), 394 （2013）.

32. Horng, J., Chen, C. F., Geng, B., Girit, C., Zhang, Y., Hao, Z. & Shen, Y. R. Drude conductivity of Dirac fermions in graphene. *Physical Review B*, *83*(16), 165113 (2011).

33. Sun, D., Wang, M., Huang, Y., Zhou, Y., Qi, M., Jiang, M., & Ren, Z. Enhanced spatial terahertz modulation based on graphene metamaterial. *Chinese Optics Letters*, *15*(5), 051603 (2017).

34. Murayama, K., & Tomida, M. Heat-induced secondary structure and conformation change of bovine serum albumin

investigated by Fourier transform infrared spectroscopy. *Biochemistry*, 43(36), 11526-11532 (2004).

35. Dai, S., Ma, Q., Liu, M. K., Andersen, T., Fei, Z., Goldflam, M. D. & Keilmann, F. Graphene on hexagonal boron nitride as a tunable hyperbolic metamaterial. *Nat. Nanotech.*, *10*(8), nnano-2015.

Supplemental Material

Detecting molecular vibrational modes of side chains and endpoints in nanoscale proteins with graphene plasmon

Methods

Fabrication. A graphene sheet grown by chemical vapor deposition was transferred onto the MgF_2 (700 nm)/Si substrate and then patterned into nanoribbons arrays using electron beam lithography and oxygen plasma etching. Ti/Au (5 nm/60 nm) metal stacks were deposited as the source and drain electrodes after an additional electron beam lithography process were used. We deposited a 700nm thick MgF_2 film onto a low-doped Si substrate using electronic beam evaporation. 9 nm thick bovine serum albumin(BSA) layers were spinned onto the sensor as a sensing sample.

Characterization. Patterned graphene nanoribbons were characterized with scanning electron microscopy (Hitachi S-4800). The graphene quality was confirmed by Raman spectroscopy (Horiba Jobin Yvon LabRAM HR800). The electrical transport properties were characterized using a semiconductor parameter analyser (Agilent 4294A) at room temperature. The thicknesses of the protein layers were measured by ellipsometry.

Simulation. The graphene plasmon were simulated by using the finite element method. The infrared lights impinge perpendicular on graphene nanoribbons. We modelled graphene as a thin film with a thickness of t and imposed the relative permittivity $\varepsilon_G = -i\sigma/\omega\varepsilon_0 t$ is the complex optical conductivity of graphene evaluated within the local random phase approximation. The graphene thickness is set to be 1 nm, at which the calculations reach proper convergence. The enhanced 9nm thickness BSA infrared extinction is simulated in S.M. Figure 1. In Figure 2a, detection of different thickness BSA is simulated, we simulate the extinction spectra of graphene plasmon with varied protein film thickness, i.e., 4 nm, 6 nm, 8 nm and 10 nm, as shown in S.M. Figure 2a. The dips in the graphene plasmon resonant peaks (the plasmonic enhanced molecular signals) are deeper when the thickness of protein is increasing. By integrating the peaks area in S.M. Figure 2b which is the result of subtracting baseline, we get 4.35, 3.48, 2.66 and 1.69 for the film thickness of 10 nm, 8 nm, 6 nm, and 4 nm, which has linear relationship

according to S.M. Figure 2 c. In Figure 3, we simulate the detection of single BSA molecule (9nm thickness, 10nm width) with enhancement of double layered graphene plasmon, the red line is the results of single molecule that on the hotspot of double layered graphene plasmon, and the black line is the results of single molecule that not on the hotspot of double layered graphene plasmon; we can find that there are no enhancement of BSA molecule which is not putted on the hotspot of graphene plasmon, and the enhanced signal of one molecule is about five times weaker compared with the enhanced signal of single layer BSA (Figure3a in manuscript) even the molecule is putted on the hotspot, which amide I band and amide II band can be identified and the side chains and endpoints signal is too weak to identify by considering the experiment noise.

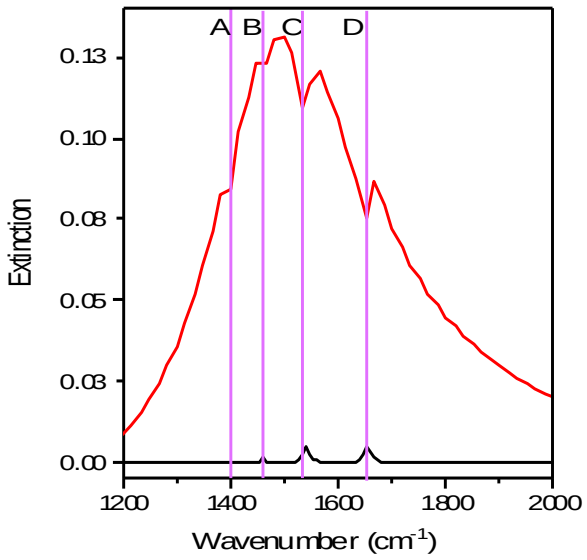

S.M. Figure1. The simulation results of 9nm BSA on double layered graphene plasmon.

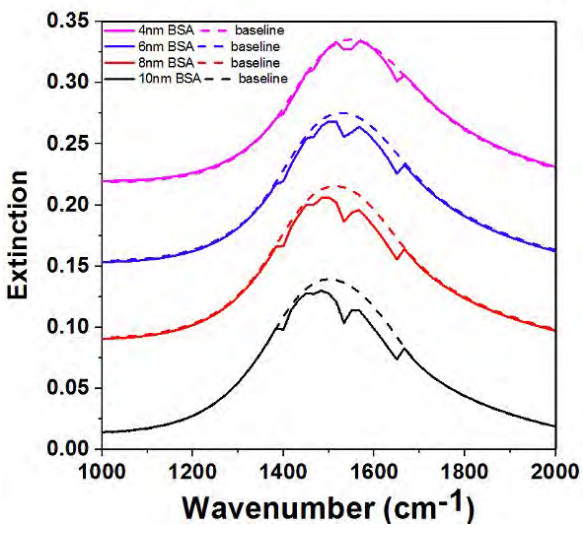

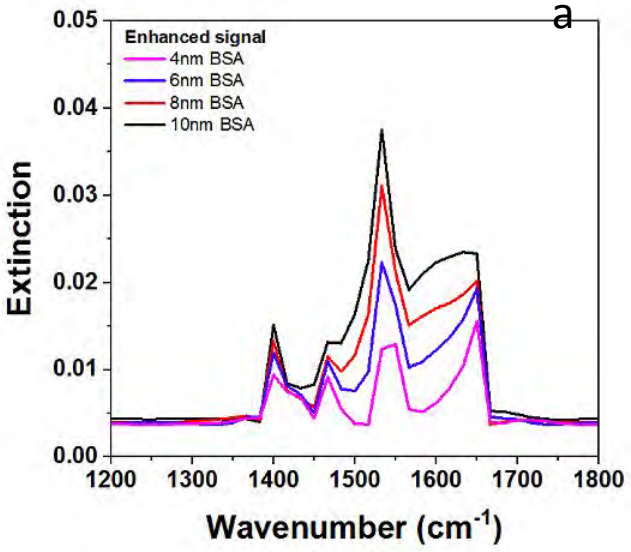

C

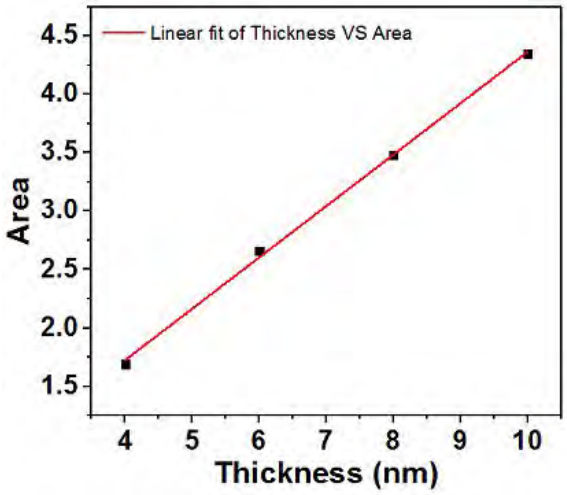

S.M. Figure2. Simulation results: (a) Extinction spectra of the DL-GNR after the protein layer formation at different BSA thickness (4nm, 6nm, 8nm, 10nm- solid lines). The baselines derived from the pristine plasmon extinction spectra are shown as dashed lines. (b) The plasmonic enhanced signal at different BSA thickness were obtained by subtracting the corresponding baseline from each simulated extinction curve in (a). (c) Area of integrated peaks versus thickness of protein.

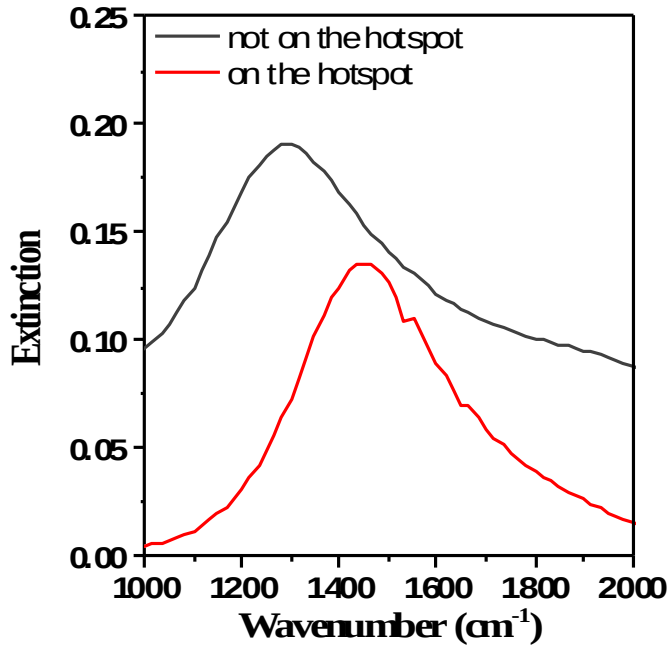

S.M. Figure3. Simulation results: Single BSA molecule enhanced detection when it is putted on/not on the hotspot of double layered graphene plasmon.

FTIR microscopy measurements. Infrared transmission measurements were performed using a FTIR microscopy (Thermo Fisher Nicolet iN10). We generated a background spectrum for each measurement. A bare MgF_2/Si substrate was used to extract the background signal from the pristine 9 nm thick protein film absorption spectrum. A single-beam transmittance spectrum collected at the charge neutral point (T_{CNP}) was used as the background spectrum and the single-beam transmittance spectrum (T) at each gate voltage was measured to obtain the extinction spectrum using the equation $1 - T/T_{CNP.}$ In S.M. Figure4a, the extinction spectrum of double layered graphene plasmon before the protein layer formation is given, and the substrate signal of 700nm MgF_2 is in the S.M. Figure4b.

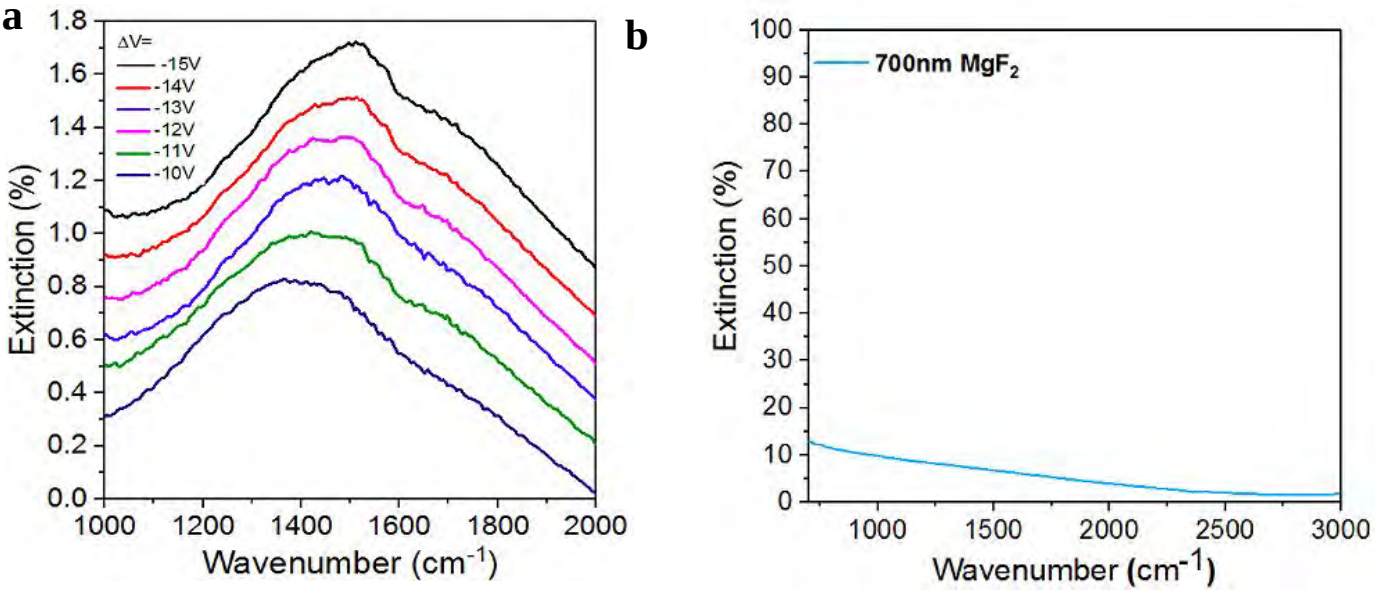

S.M. Figure 4. (a) Extinction spectra of the double layered graphene plasmon before the protein layer formation. (b) Extinction spectra of substrate 700nm MgF_2.